Proceedings of the InterPACK 2020
International Mechanical Engineering Congress and Exposition
IMECE2019
October 27-29, 2020, Anaheim, CA, USA

InterPACK 2020

LOCAL HEAT ENERGY TRANSPORT ANALYSES IN GALLIUM-INDIUM-NITRIDE/GALLIUM NITRIDE HETEROSTRUCTURE BY MICROSCOPIC RAMAN IMAGING EXPLOITING SIMULTANEOUS IRRADIATION OF TWO LASER BEAMS

Shungo Okamoto[1], Naomichi Saito[1], Kotaro Ito[1], Bei Ma[1], Ken Morita[1], Daisuke Iida[2], Kazuhiro Ohkawa[2], Yoshihiro Ishitani[1]

[1]Chiba University, Chiba City, Japan
[2] King Abdullah University of Science and Technology, Thuwal, Saudi Arabia

ABSTRACT

Local heat transport in two $Ga_xIn_{1-x}N$/GaN-heterostructures on sapphire substrates is investigated by microscopic Raman imaging using two lasers of 532 nm (Raman observation) and 325 nm (heat generation and Raman observation), which enables the separation of heat generation and Raman observation positions. It is found that E_2(high) and A_1(LO) modes of the $Ga_{0.84}In_{0.16}N$ layer exhibit mutually different characteristics, which indicates the analysis of the occupation of the A_1(LO) mode is available. E_2(high) mode of the GaN layer observed by the 532-nm laser reveals that the transport of the heat energy generated in the $Ga_{0.84}In_{0.16}N$ layer to the GaN under layer is blocked in the high-density area of misfit dislocation in the vicinity of the heterointerface.

Keywords: Phonon transport, Raman imaging, III-nitrides

1. INTRODUCTION

It is known that the operating characteristics of electronic devices deteriorate with increasing temperature [1-3]. For the ultraviolet emission mechanism, for example, the population distribution in excitonic states varies depending on phonon occupation or phonon temperature, and an expansion of the population distribution reduces the excitonic emission rate and efficiency [4-7]. Electron scattering in transistors yields device heating, which increases the rate of electron scattering by phonons. III-nitrides, which are utilized for visible – ultraviolet LED, laser diodes, and high electron mobility transistors, have high interaction strength with longitudinal optical (LO) phonon. In many cases, these crystals are grown on a substrate with high lattice mismatch, which means the existence of high-density crystal defects in the vicinity of the interface with the substrate. Previously, a lot of discussions have been conducted on the effects of crystal defects on thermal energy transport. Some references indicate that threading dislocations give eminent effects on energy transport when the density is over 10^8 – 10^{10} cm^{-2} [8, 9]. One such article indicates that voids are major defects suppressing thermal transport [10]. However, microscopic local imaging of heat transport at a specific defect is still a challenging issue.

The radiation efficiency of exciton is reduced by the population distribution among the principal quantum number states induced mainly by the strong interaction with LO phonons [4-7]. This result indicates that it is necessary to analyze the transport of LO phonons separately from acoustic phonons. In Raman measurements, mode-separated phonon properties can be obtained, which is an advantage compared with the pump-probe method of photoreflectivity [11, 12]. It is known that in Raman scattering measurements, two spectra obtained using two laser beams of different wavelengths provide the depth profile of the strain field of a two-layer stacking structure [13], while analyses of heat transport at a heterointerface or crystal defects require the additional element of simultaneous incidence of two laser beams, the pump (heating) and probe (Raman measurement) system, and the control of irradiation positions in order to distinguish the heating and probing areas. Micro-Raman mapping has been utilized for the analysis of spatially local temperatures [14,15] and heat generation in transistors [15-18]. Various methods including this technique have been studied for the analysis of heat transport across heterointerfaces or superlattices [19-27]. However, microscopic local imaging of mode-separated phonon transport at a specific defect is still a challenge.

GaInN and AlInN alloys are future materials for high power transistors and optical devices in the green gap in laser devices. Characteristic properties of local strain, fluctuation of energy gap due to spatial nonuniformity of alloy composition, carrier dynamics, and so forth are now under investigation, while nonuniform thermal conduction remains unclear. As the difference in lattice constant at a heterointerface extends to 14 %, which is for AlN and InN, misfit dislocations can be generated in the vicinity of the heterointerfaces [28, 29].

 © 2020 by ASME

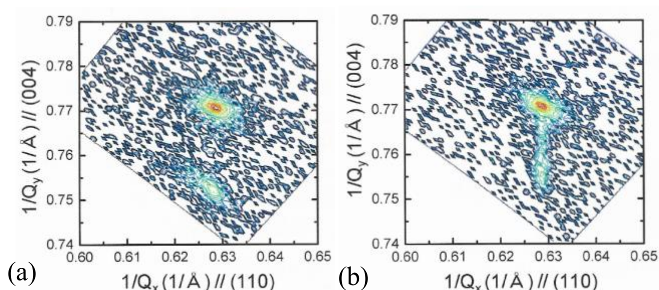

FIGURE 1: RECIPROCAL LATTICE SPACE MAPPING BY X-RAY DIFFRACTION FOR SAMPLE A (a), AND SAMPLE B (b).

In the previous letter, we have substantialized the advantage of our pump (heating) – probe (Raman measurement) method using a sample with misfit dislocations (MDs) at a GaInN/GaN heterointerface. In this paper, we contrast the characteristic properties of the heat transport at the heterointerface including MDs with the properties of a sample with a far lower density of MDs. In the previous report, we have not discussed the difference in the probed physical process between phonon modes. In this report, Raman imaging results of the A_1(LO) mode (A_1^L) are discussed in comparison with the results on the E_2(high) mode (E_2^H), and the discussion is extended to the characteristic properties of the LO phonon transport.

2. MATERIALS AND METHODS

Two $Ga_xIn_{1-x}N$ samples A and B with a thickness of 110 nm were grown on n-GaN layers on sapphire substrates by a metal-organic vapor phase epitaxy system [31, 32]. Sample A has an alloy composition x = 0.84 for the crystal under the pseudomorphic condition. Sample B has graded x, which is continuously varied from 0 to 0.17 toward the surface. No layer with any constant x is included. FIGURE 1 shows reciprocal lattice space mapping images. The broad diffraction image of the $Ga_xIn_{1-x}N$ layer of sample A indicates that the crystal is partially relaxed. The result for sample B indicates that $Ga_xIn_{1-x}N$ is subject to pseudomorphic growth. No geometrical surface structure was found in the optical microscope image or scanning electron microscope image for these samples. An infrared (IR) reflectance analysis for the LO phonon – plasmon coupling mode

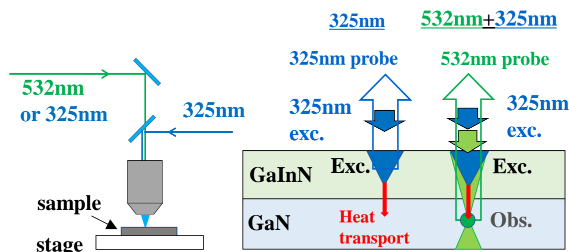

FIGURE 2: SCHEMATIC OF LASER IRRADIATION ON A SAMPLE AND CROSS-SECTIONAL DIAGRAM OF HETAT GENERATION (Exc.) AND RAMAN OBSEVATION (Obs.) IN THE MEASUREMENT SYSYTEM USING TWO LASERS.

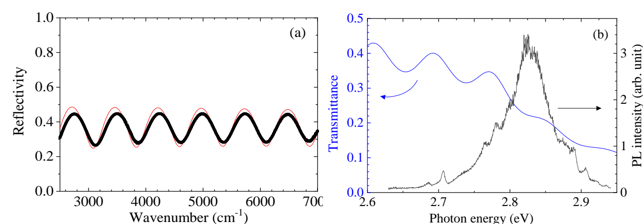

FIGURE 3: INFRARED REFLECTANCE SPECTRA IN IR REGION (a), AND EXAMPLE OF EXPERIMENTAL PL SPECTRA WITH CALCULATED TRANSMISSION SPECTRUM (b). THE THICK BALCK AND RED CURVES IN (a) SHOW THE EXPERIMENTAL SPECTRUM AND THE BEST-FIT THEORETICAL CURVE USING TRASFER MATRIX METHOD.

revealed that the residual electron density of this film of sample A was approximately 6×10^{17} cm^{-3}.

These samples were characterized by micro-Raman spectroscopy at 295 K with controlling spot positions of two lasers: 325 nm and 532 nm. An objective lens with NA = 0.47 and ×40 was utilized. When beams of two different wavelengths were simultaneously incident on the same point on a sample surface, the 532-nm light was focused with a diameter of approximately 0.65 μm, while the 325-nm light was diffused at an approximate diameter of 7 μm. The fluctuation of circumstance temperature was kept less than 1 degree. The Raman shift was calibrated using the 5460.7Å line of a Hg lamp. Using this system, we have observed anisotropic heat transport in the GaInN/GaN heterostructures by analyzing images of Raman signals for the E_2^H and A_1^L in 8 – 15 μm square regions. FIGURE 2 shows the geometric condition of the laser irradiation on a sample and the cross-sectional schematic of heating and Raman probing. The 325-nm excitation laser is used for heat generation in the GaInN layers by the energy relaxation of photo-generated carriers to the band edges. When the same laser beam is utilized to probe the Raman signal, the energy shift of a Raman peak reveals an increase in temperature in a GaInN layer. When the Raman signal is probed by the 532-nm laser, which penetrates to the GaN underlayer, the increase in the temperature of the GaN layer is probed. The relaxation energy of excited carriers to the band bottoms is expected to be 27 % of the excitation energy for sample A. For sample B, generated energy is estimated to be 30 % of that of sample A. Further energy transfer to the lattice vibration system is possible through nonradiative carrier recombination. The density of free carriers generated by a 1mW excitation of the 325-nm beam was estimated to be approximately 5.55×10^{13} cm^{-2} (5×10^{18} cm^{-3} for sample A) or less by considering the lifetime of shorter than 500 ps. Carrier diffusion in the $Ga_xIn_{1-x}N$ layers further decreases the carrier density to approximately one quarter. In simultaneous excitation, the carrier density is estimated to be less than 10^{17} cm^{-3} for the excitation laser power of 10 mW for sample A. In these cases, the thermal energy conduction by free carriers can be neglected [9]. In sample B, the generated carriers are estimated to be confined in the vicinity of the surface.

© 2020 by ASME

3. RESULTS AND DISCUSSION

3.1 Photoluminescence properties

FIGURE 3(a) shows an infrared reflectance spectrum of sample A, where the incidence angle is 60° from the surface normal. In the observed energy region, the electric permittivity is nearly constant. The theoretical spectrum fitted using the relative dielectric constant at the infinite frequency of 5.35 is plotted by the red line, which satisfactorily agrees with the experimental result. The film thickness values of the GaInN and GaN were obtained to be 110 nm and 3060 nm. The transmission spectrum was calculated using these parameters. FIGURE 3(b) shows an example of the photoluminescence (PL) spectra observed using an excitation laser of 325 nm and the calculated transmission spectrum for sample A. The amplitude of the spectrum oscillation by the optical interference in the transmission spectrum is decreasing with the increase in the photon energy. The PL spectrum is found to be scarcely affected by optical interference. FIGURE 4 shows PL intensity mappings. For sample A, dark lines parallel to $\langle 1\bar{1}00 \rangle$ intersect mutually at an angle of 60°. This contrast in PL intensity is attributed to nonradiative carrier recombination (NR) in the vicinity of MDs on the $Ga_{0.84}In_{0.16}N$/GaN interface. For sample B, the PL was found to be peaked at 2.88 eV with a width of approximately 80 meV. The mapping image shows no dark line, which indicates MDs are not observed in this region.

3.2 Mode dependent energy transport properties in GaInN layers

FIGURE 5 shows examples of Raman spectra. In FIGURE 5(b), the Raman spectrum obtained by the 532-nm laser is also exhibited by the blue curve, which is dominated by the signal from the n-GaN layer. In FIGURE 5(a), the obtained spectrum peak energies are shifted from those of the n-GaN substrate. Further, as the 325-nm laser light is absorbed within the depth of approximately 100 nm from the surface, the observed Raman peaks by using this laser for sample A are attributed to the E_2^H and A_1^L modes of the GaInN layer. In FIGURE 5 (b), the E_2^H signal obtained by the 325-nm laser is overlapped with the signal by the 532-nm laser, whereas the A_1^L signal by the 325-nm laser is shifted from the broad LO phonon – plasmon coupled (LOPC) mode peak of the n-GaN layer. Using the concerned deformation potentials of $Ga_xIn_{1-x}N$ obtained by the linear interpolation between the values of GaN and InN listed in Table I [33-39], and the mode energies of relaxed materials [40, 41], the mode

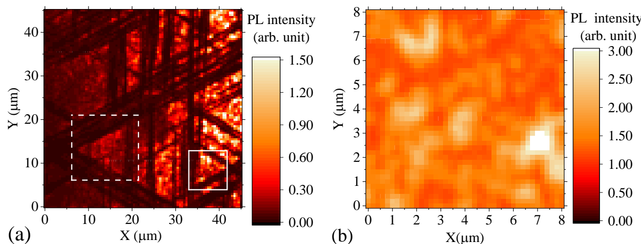

FIGURE 4: MAPPING IMAGES OF PL SPECTRUM INTENSITY FOR SAMPLE A (a) [30] AND SAMPLE B (b).

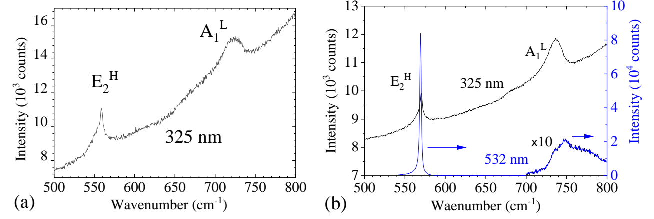

FIGURE 5: RAMAN SPECTRUM EXAMPLES USING THE 325-NM EXCITATION FOR SAMPLE A (a) [30] AND SAMPLE B (b).

energies of strained materials were calculated. As a result, pseudomorphic $Ga_xIn_{1-x}N$ alloys in the alloy composition range of $0.83 \le x \le 1.0$ have E_2^H energy in the range of 567 – 576 (cm^{-1}), and A_1^L energy in the range of 736 – 728 (cm^{-1}). Thus, the observed A_1^L peak by the 325-nm laser for sample B is attributed to the superposition of the signals from various $Ga_xIn_{1-x}N$ crystals in the range of $0.83 \le x \le 1.0$. For the E_2^H peak, although the E_2^H phonon energies of pseudomorphic $Ga_xIn_{1-x}N$ in $0.83 \le x \le 1.0$ are included in a small range of 9 cm^{-1}, we can not exclude the possibility that the spectrum peak includes the signal generated by the small fraction of the laser light penetrated to the n-GaN. In this case, the signal probes the phonon modes in the region of less than 100 nm from the interface with the GaInN layer, which indicates that the temperature increase in a small region of GaN facing the GaInN possibly affects the signal.

The mapping images of these peak energies in the dashed square region of sample A in FIGURE 4 are shown in FIGURE 6. The images of the E_2^H mode show the same triangular shape as observed in the PL intensity mapping, which indicates that the InN mole fraction or the magnitude of the strain depends on the density of MD. By increasing the intensity of the 325-nm excitation laser from 1.1 to 11 (mW), the mode energy is found to be decreased, and the contrast of the triangular structure

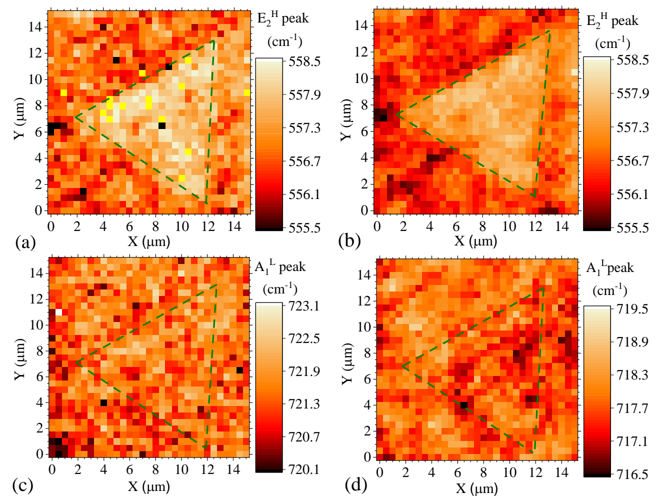

FIGURE 6: MAPPING IMAGES OF THE E_2^H (a) [30] AND (b) [30], AND A_1^L (c) AND (d) OF THE GaInN LAYER. (a) AND (c) ARE FOR THE EXCITATION POWER OF 1.1 mW, AND (b) AND (d) ARE FOR 11 mW.

© 2020 by ASME

TABLE 1: PARAMETERS FOR ANISOTROPIC STRAIN AND LATTICE VIBRATION OF GaN AND InN.

		a (cm^{-1})	b (cm^{-1})	ν	$\alpha_{th//}$ (10^{-6} K^{-1})	dω/dT (10^{-2} cm^{-1}K^{-1})	ω_0 (cm^{-1})
GaN	E_2^H	-742 [33]	-715 [33]	0.183[34]	4.2 [37]	-0.87 [34]	568.5 [33], 567.6 [39]
	A_1^L	-664 [33]	-882 [33]	0.25-0.33 [33]		-2.4 [33]	736.4 [33]
InN	E_2^H	-938 [35]	-407 [35]	0.21 [35]	3.83 [36]	-13 [38]	494.6 [35]
	A_1^L	-901 [35]	-587 [35]	0.27 [34]		-6.0 [38]	582.3 [35]

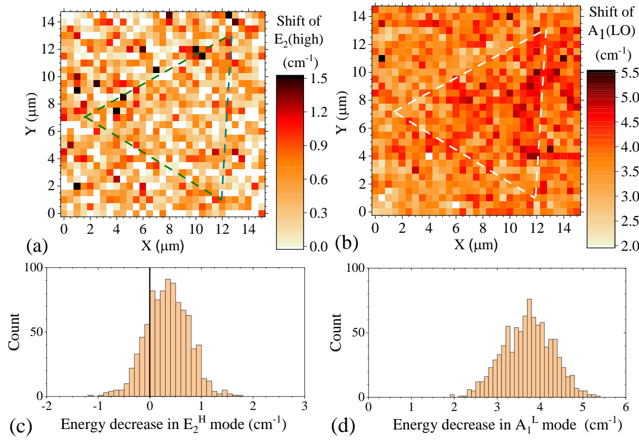

FIGURE 7: MAPPING IMAGES OF THE DECREMENTS OF THE MODE ENERGIES BY INCREASING THE 325-nm LAER POWER FOR THE E_2^H (a)[30] AND A_1^L (b), AND HISTOGRAMS OF THE DECREMENTS IN THE OBSERVED AREA FOR THE E_2^H (c)[30] AND A_1^L (d).

becomes clear as shown in FIGURE 6(b). This result indicates the crystal temperature increases by increasing the laser intensity. In contrast to this result, the images of the A_1^L in FIGURE 6(c) and (d) show no clear triangular structure even by increasing the excitation power to 11 mW. At a further lower excitation power of 0.1 mW, the A_1^L peak energies inside and outside the triangular structure were measured, because imaging measurement requires too much time when using such a low excitation laser intensity. As a result, it was found that the energy of this mode inside the triangle is greater than that outside the triangle. Thus, the A_1^L energies at the low excitation power limit show a property consistent with the mapping image for the E_2^H. FIGURES 7 (a) and (b) show the decrements in the respective mode energies by increasing the laser power. The decrement in the A_1^L energy is greater than that in the E_2^H mode energy. This phenomenon can not be attributed to LOPC. This is because both of the energies of the higher and lower energy branches of the LOPC modes increase with the increase in the electron density. FIGURES 7 (c) and (d) show histograms of the variations of the mode energies, which indicate the shift of the mean mode energy of the A_1^L is seven times greater than that of the E_2^H. This result indicates that a phenomenon peculiar to the A_1^L is observed.

Candidate factors affecting this phenomenon are an extraordinal increase in the occupation factor of the A_1^L by heating and the greater shift of the Raman peak energy of the A_1^L. The parameters to analyze the mode energies are listed in Table I. We assume that the shift of mode energy $\Delta\omega$ by strain is expressed as $2a\varepsilon_{xx} + b\varepsilon_{zz}$, which is transformed to

$$\Delta\omega = [2a - 2b\nu/(1-\nu)]\, \varepsilon_{xx} \quad (1)$$

Here, ε_{xx}, ε_{zz}, and ν are strains in x and z directions, and Poisson ratio, respectively. The notations of a and b are the deformation potentials. When we adopt the potential values of a = 742 cm^{-1} and b = 715 cm^{-1} for the E_2^H, ν = 0.25 for GaN, and the mode energies for $Ga_xIn_{1-x}N$ alloys in references 40 and 41, the observed mode energy for the E_2^H is lower than the calculated pseudomorphic $Ga_{0.84}In_{0.16}N$ layer, although the computed value of the A_1^L is consistent to the experimentally observed mode energy. This result indicates that the crystal is relaxed to some extent even inside the triangular shape region, and that the A_1^L energy is affected by LOPC originating from the photoexcited electrons, while the temperature increase affects the peak energy shift of the A_1^L dominantly. Here, the parameters of $Ga_xIn_{1-x}N$ excluding mode energies were obtained by the linear interpolation of the values of GaN and InN.

When we assume that the temperature increase of the sapphire substrate excluding the vicinity of the interface is negligible, and the Poisson ratio is constant, the energy shift of the E_2^H peak by increasing the laser power of 325 nm, $\Delta E(E_2^H)$, is expressed in the following equation by considering the thermal strain.

$$\Delta E(E_2^H) \approx \Delta E(E_2^H\!: T - T_0, 0) - C_E \cdot \alpha_{th\,//} \cdot (T - T_0) \quad (2)$$

Here, C_E is the coefficient presenting the dependence of mode energy on in-plane strain ε_{xx} shown in Eq. (1). The linear thermal expansion coefficient is denoted as $\alpha_{th\,//}$. $\Delta E(E_2^H\!: T-T_0, 0)$ is the decrease in the mode energy by increasing temperature from T_0 to T for bulk crystal without thermal stain. $\Delta E(E_2^H)$ is found to be $2.4\times10^{-3}\cdot\Delta T$ (cm^{-1}) using the parameters in Table I. The energy shift of 0.5 cm^{-1} for the E_2^H of sample A corresponds to a temperature increase of 21 K with an increase in the excitation power of the 325-nm light, whereas the increase for the A_1^L mode is calculated to be 130 K at least. As no notch filter for the 325-

© 2020 by ASME

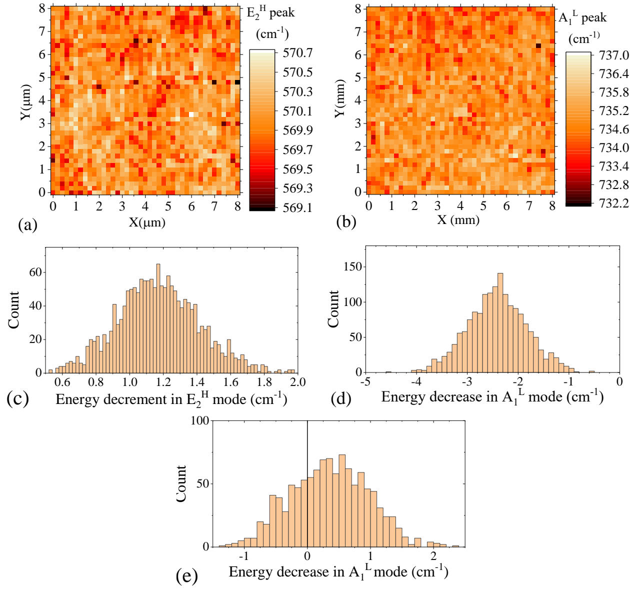

FIGURE 8: MAPPING IMAGES OF RAMAN PEAK ENERGIES FOR THE E_2^H (a) AND A_1^L (b) BY THE 325-nm EXCITATION (10 mW) FOR SAMPLE B, AND THE DECREMENTS IN THE MODE ENERGIES BY INCREASING THE EXCIATATION POWER FROM 1 mW TO 10 mW FOR E_2^H (c) AND A_1^L (d), AND FROM 2 mW TO 5 mW FOR A_1^L (e).

nm excitation was available in the present experiment, the ratio of Anti-Stokes and Stokes signal intensities was not investigated. Instead, this intensity ratio is discussed using an InN film (4.5-µm thickness) on a GaN layer and the 532-nm laser, where the intensity ratio of anti-Stokes (I_{AS}) and Stokes (I_S) signals were investigated using the following equation.

$$\frac{I_{AS}}{I_S} = \left(\frac{\omega_0+\omega_{ph}}{\omega_0-\omega_{ph}}\right) \exp\left(-\frac{\hbar\omega_{ph}}{k_b T}\right) \quad (3)$$

Here, ω_0, ω_{ph} , k_b , and T are the frequency of the incident laser, phonon frequency, Boltzmann factor, and temperature, respectively. Since the energy gap of the InN layer is 0.63 eV at room temperature [42], the excitation using the 532-nm laser provides enough carrier relaxation energy. When the excitation energy was increased from 14 to 20 (mW), we have found a temperature increase from 311 to 316 (K) for the A_1^L, while no temperature increase for the E_2^H. Thus, the occupation of the A_1^L

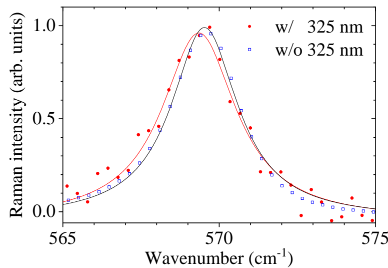

FIGURE 9: SPECTRA OF THE E_2^H WITH AND WITHOUT THE 325-nm EXCITATION[30].

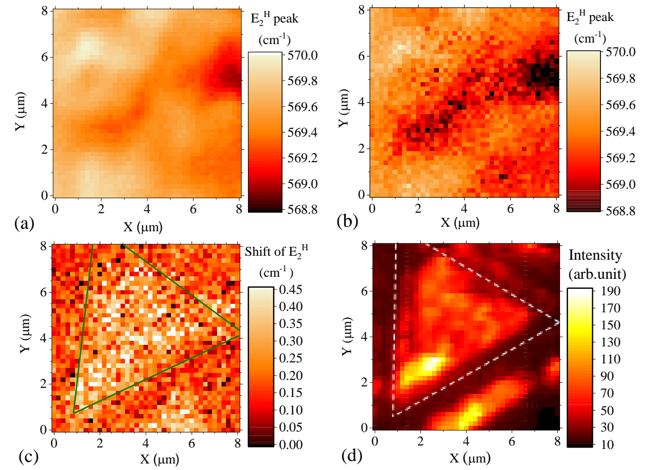

FIGURE10: RAMAN IMAGES BY THE 532-nm LASER WIHTOUT (a)[30] AND WITH (b) THE 325-nm LAER IRRADIATION, AND DECREMENT OF THE PEAK ENERGY BY IRRADIATING THE 325-nm LAESR (c)[30]. MAPPING OF THE PL INTENSITY FROM THE GaInN LAYER IS PLOTTED IN (d)[30].

is thought to be increased by the electronic band to band transition and the subsequent carrier energy relaxation. It is thought that this phenomenon can not be attributed to a mechanism based on any temperature increase originating from the increase in the occupation factor of acoustic phonon modes, which induces the lattice dilatation and the resultant decrease in energy of every phonon mode.

The featureless images of the decrement of the Raman peak energies shown in FIGURE 7 indicate that thermal energy transport is independent of the defects on the $Ga_xIn_{1-x}N$/GaN interface. Two mechanisms are considered: (1) long diffusion length of thermal energy with respect to the size of the triangle and (2) dominant thermal conduction on the surface side $Ga_xIn_{1-x}N$ layer with higher crystal quality than that of the crystal in the vicinity of MDs located on the heterointerface. In PL analysis, it was found that the PL spectra in the dark PL region in FIGURE 4 have another peak at 2.75 eV, which indicates that the PL peak at 2.82 eV originates from the crystals with improved quality. In the dark region, this PL component originating from the improved crystal quality is included, which suggests that the quality of crystal in the vicinity of the surface is improved even in the dark PL region. The energy transport along this improved crystal regions possibly induces long heat energy diffusion over the size of the triangle.

FIGURE 8 shows the Raman mapping images for sample B, where the triangle shape is not observed, which is consistent with the result of the PL mapping image shown in FIGURE 4 (b). The histograms of the decrements of the two mode energies are shown in FIGURES 8 (c), (d), and (e). As the observed Raman peak in the vicinity of 570 cm^{-1} is possibly the overlap of the peaks for the GaInN and GaN layers, the temperature of the GaInN layer or the GaN in the vicinity of the GaInN layer is increased by 170 K at least. At present, the reason for this high

© 2020 by ASME

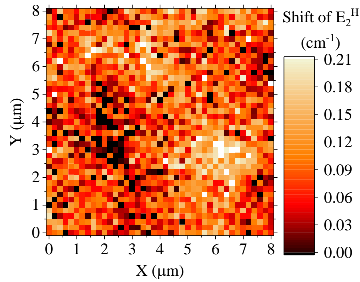

FIGURE 11: MAPPING IMAGE OF THE DECREMENT OF THE E_2^H PEAK ENERGY OF SAMPLE B BY IRRADIATING THE 325-nm LAESR.

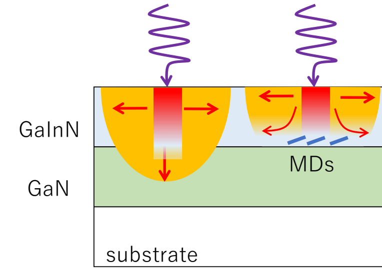

FIGURE 12: SCHEMATIC OF THE BLOCKING OF HEAT ENERGY TRANSPORT IN THE EXTENT OF MDS ON THE HETEROINTERFACE.

temperature increase is not solved. However, phonon confinement in the region with lower x (lower phonon mode energy) in the $Ga_xIn_{1-x}N$ layer with graded alloy composition may be a candidate reason. On the other hand, the A_1^L energy increases by increasing the power from 1 to 10 (mW), while the decrease in the mode energy is observed for a small increase in the excitation power from 2 to 5 (mW) as shown in FIGURE 8(e). These results indicate that the temperature increase takes place also for the A_1^L. As carrier confinement in the vicinity of the surface in this sample takes place, the increase in the LOPC mode energy is dominant when the excitation power is high. Thus, the analysis for the A_1^L is complicated because of the two effects of an increase in temperature and an increase in electron density.

3.3 Energy transport from the GaInN layer to the underlying GaN

FIGURE 9 shows an example of Raman spectra obtained by the 532-nm line with and without the simultaneous irradiation of the 325-nm laser for sample A. The spectrum peak at approximately 569 cm^{-1} is attributed to the E_2^H mode of the GaN film. FIGURES 10 (a) and (b) show the mapping images of the peak energy obtained by Lorentzian fitting for the region indicated by the white solid square line in FIGURE 2. The variation in the mode energy in this area is within 1.1 cm^{-1}, which corresponds to the strain variation of approximately 0.12 %. When the 325-nm light with a power of 20 mW is incident on the sample, the mode energy is found to shift to the lower energy side, which indicates an increase in temperature. The obtained mapping of the decrement in the mode energy is plotted in FIGURE 10(c). The observed image exhibits the same triangular structure as observed in the PL intensity image shown in FIGURE 10(d) and the image of the E_2^H energy of the GaInN layer. The decrease in the E_2^H energy of the GaN film in the bright PL region is more significant than that in the area including MDs and exhibiting low PL intensity. This result indicates that the temperature increase in the GaN region under the GaInN layer with lower MD density is higher than that in the area outside the triangle rim with a higher density of MDs. The increase in temperature within the triangle is estimated to be approximately 56 K, which is an average value in the region probed by the 532-nm light. Detail investigation on thermal strain and the physical parameters are required for further analysis.

FIGURE 11 shows the mapping image of the decrement of the E_2^H energy by irradiating the 325-nm light on sample B. The measurement area is not the same as the area in FIGURE 4(b) or FIGURE 8. No MD structure is observed for this sample. The magnitude of the decrease in the E_2^H energy is approximately a half of that for sample A. It is estimated that the smaller decrement in the mode energy for sample B originates from the lower relaxation energy of carriers in the GaInN layer of sample B, while for the further quantitative discussion, it is required to investigate the phonon transport in the GaInN layer with graded alloy composition and phonon generation by nonradiative carrier recombination.

The schematic of the heat transport in the present samples is depicted in FIGURE 11. It is believed that the extent of MDs blocks the heat transport from the GaInN layer to the underlying GaN, while lateral heat transport in the $Ga_xIn_{1-x}N$ layer of sample A takes place primarily via the crystal in the surface side region with improved crystal quality.

4 CONCLUSION

The Raman imaging using two lasers with different wavelengths is practical to analyze the heat energy transport at heterointerfaces. We have found the heat energy transport through the GaInN/GaN interface is blocked at MDs. Further, LO phonon can be separately analyzed from the energy transport observed for the E_2^H mode, where it is required to discuss the two factors of the temperature increase and the increase in electron density. We have found that LO phonon transport property is quite different from that of the E_2^H.

ACKNOWLEDGEMENTS

This study was partly supported by the Grant-in-Aid for Scientific Research of the Japan Society for the Promotion of Science (16H06425 and 17H02772) and King Abdullah University of Science and Technology (KAUST) (BAS/1/1676-01-01)

REFERENCES

[1] I. Jabbari, M. Baira, H. Maaref, and R. Mghaieth, Physica E **104**, 216 (2018).

© 2020 by ASME

[2] C. Gaquière, H. Maaref , J. Phys. Chem. Sol. **132,** 157 (2019).
[3] M. S. Ferdous, X. Wang, M. N. Fairchild, and S. D. Hersee, Appl. Phys. Lett. **91**, 231107 (2007).
[4] Y. Ishitani, K. Takeuchi, N. Oizumi, H. Sakamoto, B. Ma, and K. Morita, H. Miyake, and K. Hiramatsu, Journal of Physics D **49**, 245102 (2016).
[5] K. Oki, B. Ma, and Y. Ishitani, Phys. Rev. B **96**, 205204 (2017).
[6] Y. Ishitani, K. Oki, and H. Miyake, Jpn. J. Appl. Phys. **58**, SCCB34 (2019).
[7] K. Oki and Y. Ishitani, Journal of Applied Physics **125**, 205705 (2019).
[8] J. Ma, X. Wang, B. Huang, and X. Luo, J. Appl. Phys. **114**, 074311 (2013).
[9] T. E. Beechem, A. E. McDonald, E. J. Fuller, A. A. Talin, C. M. Rost, J.-P. Maria, J. T. Gaskins, P. E. Hopkins, and A. A. Allerman, J. Appl. Phys. **120**, 095104 (2016).
[10] R. Aghababaei, G. Anciaux, and J.-F. Molinari, , Appl. Phys. Lett. **105**, 194102 (2014) .
[11] G. Chen and M. Neagu, Appl. Phys. Lett. **71**, 2761 (1997).
[12] R. Anufriev, A. Ramiere, J. Maire, and M. Nomura, Nat. Commun. **16**, 15505 (2017).
[13] G. Zeng, P. Harrison, A. Kidman, A. Almebir, L. Feng, and J. Wu, Appl. Spectr. **70**, 1555 (2016).
[14] X. Tang, S. Xu, and X. Wang, Plos one **8**, e58030 (2013).
[15] M. Kuball, S. Rajasingam, A. Sarua, M. J. Uren, T. Martin, B. T. Hughes, K. P. Hilton, and R. S. Balmer, Appl. Phys. Lett. **82**, 124 (2003).
[16] M. Kuball, G. J. Riedel, J. W. Pomeroy, A. Sarua, M. J. Uren, T. Martin, K. P. Hilton, J. O. Maclean, and D. J. Wallis, IEEE Elec. Devices Lett. **28**, 86 (2007).
[17] R. J. Simms, J. W. Pomery, M. J. Uren, T. Martin, and M. Kuball, Appl. Phys. Lett. **93**, 203510 (2008).
[18] C. Hodges, J. Pomeroy, and M. Kuball, J. Appl. Phys. **115**, 064504 (2014).
[19] B. Saha, Y. R. Koh, J. Comparan, S. Sadasivam, J. L. Schroeder, M. Garbrecht, A. Mohammed, J. Birch, T. Fisher, A. Shakouri, and T. D. Sands, Phys. Rev. B **93**, 045311 (2016).
[20] Z. Liang, K. Saikumar, and P. Keblinski, Phys. Rev. Lett. **113**, 65901 (2014).
[21] G. Chen and M. Neagu, Appl. Phys. Lett. **71**, 2761 (1997).
[22] S.-M. Lee, D. G. Cahill, and R. Venkatasubramanian, Appl. Phys. Lett. **70**, 2957 (1997).
[23] K. Kazan, Appl. Phys. Lett. **95**, 141904 (2009).
[24] Z. Su, L. Huang, F. Liu, J. P. Freedman, L. M. Porter, R. F. Davis, and J. A. Malen, Appl. Phys. Lett. **100**, 201106 (2012).
[25] E. Ziade, J. Yang, G. Brummer, D. Nothern , T. Moustakas, and A. J. Schmidt, Appl. Phys. Lett. **107**, 091605 (2015).
[26] A. Pansari, V. Gedam, and B. K. Sahoo, J. Phys. Chem. Sol. **87**, 177 (2015).
[27] Th. Pavloudis, K. Termentzidis, Ph. Komninou, C. D. Latham , P. R. Briddon, and J. Kioseoglou, J. Appl. Phys. **119**, 074304 (2016).
[28] M. Iwaya, T. Yamamoto, D. Iida, Y. Kondo, M. Sowa, H. Matsubara, K. Ishihara, T. Takeuchi, S. Kamiyama, and I. Akasaki, Jpn. J. Appl. Phys. **54**, 115501 (2015).
[29] T. Sugiyama, Y. Kuwahara, Y. Isobe, T. Fujii, K. Nonaka, M. Iwaya, T. Takeuchi, S. Kamiyama, I, Akasaki, and H. Amano, Appl. Phys. Exp. **4**, 015701 (2011).
[30] S. Okamoto, N. Saito, K. Ito, B. Ma, K. Morita, D. Iida, K. Ohkawa, Appl. Phys. Lett. **116**, 142107 (2020).
[31] K. Ohkawa, F. Ichinohe, T. Watanabe, K. Nakamura, and D. Iida, J. Cryst. Growth **512**, 69 (2019).
[32] K. Ohkawa, Y. Uetake, M. Velazquez-Rizo, and D. Iida, Nano Energy **59**, 569 (2019).
[33] M. Kuball and J. W. Pomeroy, IEEE Trans. Dev. Mat. Reliability **16**, 667 (2016).
[34] M. A. Moram, Z. H. Barber, and C. J. Humphreys, J. Appl. Phys. **102**, 023505 (2007).
[35] X. Wang, S.-B. Che, Y. Ishitani, and A. Yoshikawa, Appl. Phys. Lett. **89**, 171907 (2006).
[36] K. Wang and R. R. Reeber, Appl. Phys. Lett. **79**, 1602 (2001).
[37] Y. Oshima, T. Suzuki, T. Eri, Y. Kawaguchi, K. Watanabe, M. Shibata, and T. Mishima, J. Appl. Phys. **98**, 103509 (2005).
[38] X. D. Pu, J. Chen, W. Z. Shen, H. Ogawa, and Q. X. Guo, J. Appl. Phys. **98**, 033527 (2005).
[39] V. Y. Davydov, Y. E. Kitaev, I. N. Goneharuk, A. N. Smirov, J. Graul, O. Semchinova, D. Uffmann, M. B. Smirov, A. P. Mirgorodsky, and R. A. Evarestov, Phys. Rev. **58**, 12899 (1998).
[40] M. R. Correia, S. Pereira, E. Pereira, J. Frandon, and E. Alves, Appl. Phys. Lett. **83**, 4761 (2003).
[41] R. Oliva, J. Ibáñez, R. Cuscó, R. Kudrawiec, J. Serafinczuk, O. Martínez, J. Jiménez, M. Henini, C. Boney, A. Bensaoula, and L. Artús, J. Appl. Phys. **111**, 063502 (2012).
[42] Y. Ishitani, Jpn. J. Appl. Phys. **53**, 100204 (2014).

© 2020 by ASME